

Liquid fluidization with cylindrical particles – highly resolved simulations

J.J. Derksen

School of Engineering, University of Aberdeen, Aberdeen, UK

jderksen@abdn.ac.uk

Submitted to AIChE Journal – January 2019

Revision submitted: March 2019

Accepted: March 2019

Abstract

We perform three-dimensional, time-dependent simulations of dense, fluidized suspensions of solid cylindrical particles in a Newtonian liquid in fully periodic domains. The resolution of the flow field is an order of magnitude finer than the diameter of the cylindrical particles. At their surfaces no-slip conditions are applied through an immersed boundary method (IBM), coupled to the lattice-Boltzmann method that is used as the fluid flow solver. The marker points of the IBM are also used to detect and perform collisions between the cylinders. With these particle-resolved simulations, we study the effects of the aspect ratio of the cylinders and the solids volume fraction on the superficial slip velocity between fluid and solids, on the solids velocity fluctuations, as well as on the orientation of the cylinders. The aspect ratio (length over diameter of the cylinders) ranges from 0.5 to 4, the solids volume fraction goes up to 0.48. Reynolds numbers based on average settling velocity are of the order of 1 to 10. At constant Archimedes number, we observe only minor sensitivities of the settling Reynolds number on the aspect ratio.

Keywords

Solids suspension, particle-resolved simulations, non-spherical particles, cylinders, lattice-Boltzmann method, liquid fluidization.

Introduction

Solid particles carried by fluid flow are a ubiquitous phenomenon in nature as well as in engineering. Practical relevance and a rich spectrum of physical phenomena have motivated extensive research in solid-fluid suspensions. One of the branches of research aims at predicting suspension dynamics through computer simulations. These are based on numerically solving mass, momentum and energy balances of the fluid phase as well as the dynamical equations of the solids phase and on coupling the phases in a meaningful manner.

There are – generally speaking – three levels of detail at which suspension simulations can be performed. At the first and most resolved level, the fluid flow is simulated at a spatial and temporal resolution that is sufficient to capture the flow around individual particles. The solid particle surfaces act as moving no-slip conditions for the fluid flow. The numerical flow solution directly provides the hydrodynamic forces and torques on the particles that are then used to integrate their equations of linear and rotational motion. Such *particle-resolved* simulations are usually performed on fixed grids that need to be much finer – by at least one order of magnitude in each coordinate direction – than the size of the particles. This resolution requirement limits particle-resolved simulations to relatively small systems with currently up to order one million particles.¹

To accommodate larger-scale systems with many more particles, one option is to coarsen the grid on which the fluid flow is solved. If in this process grid spacings become of the order of the particle size or larger, we enter the realm of discrete element method / computational fluid dynamics (DEM/CFD) simulations. This is the second level of detail of suspension simulations. Given that one does not resolve the flow around individual particles anymore, hydrodynamic forces and torques on the particles are not directly available from the fluid flow solution. As a surrogate, empirical correlations are used to estimate the forces and torques as a function of local conditions: particle-based Reynolds numbers, solids volume fractions, and possibly other parameters characterizing the flow and microstructure in the direct vicinity of a particle.² Next to hydrodynamic force and torque modeling, the exchange of information between the

Eulerian (fluid flow) and Lagrangian (particle motion) components of the simulation is a topic of active research.^{3,4}

Eulerian-Eulerian (EE) simulations are the third level of detail of suspension simulations. The solids phase is treated as a continuum that penetrates the fluid phase (and vice versa). Modeling relates – among much more – to the stresses in the solids phase as well as the forces involved in the interaction between the phases.^{5,6}

It has no doubt that the shape of the solid particles has impact on the flow behavior of the solids-liquid mixture: Hydrodynamic forces and torques depend on particle shape; in collisions, momentum exchange and how it is distributed over linear and angular components depends on shape; the way (dense) suspensions structure and pack themselves also depends on the shape of the particles. Where the majority of the works on simulating solid-liquid suspensions – at all three levels of detail as identified above – assumes the particles to be of a – more or less – spherical shape, it is thus useful to explore the role of the shape of the particles on the dynamics of a suspension. In this paper we do this by means of particle-resolved simulations with particles of cylindrical shape. The choice for cylinders has a few reasons. In the first place we have – with applications in biomass conversion in mind – an interest in the flow dynamics of fiber suspensions. In the second place, there is experimental data available regarding the behavior of suspensions of cylindrical particles.^{7,8,9} Related to this, we plan on doing experiments ourselves and the availability of accurately sized cylindrical particles (e.g. to be cut from long rods) makes particles of such shape very suitable. In the third place, cylinders have only one aspect ratio (length over diameter) so that one can explore particle shape effects based on varying a single parameter.

Reports on suspension simulations with non-spherical particles are becoming commonplace in the literature. They have been applied in the context of DEM simulations by Mahajan et al¹⁰ where the focus is on gas fluidization. Particle-resolved simulations through fixed beds of non-spherical particles¹¹ provide valuable insights into the relation between the bed's micro structure and its pressure drop. Simulations resolving the flow around a steady, cylindroid particle have been used to measure

hydrodynamic forces and torques as a function of Reynolds number and angle-of-attack.¹² This data can then be used in DEM/CFD simulations to capture the dynamic interaction between solid and fluid.

Our interest is in the collective dynamical behavior of cylinder suspensions and how it depends on key dimensionless parameters: aspect ratio, solids volume fraction and particle-based Reynolds number. For this, dense assemblies of identical cylindrical particles that are free to move and rotate have been created. The flow systems are periodic in all three coordinate directions. The suspensions are brought in a fluidized state by balancing the net gravity force on the particles by an opposing body force – that can be interpreted as a vertical pressure gradient – on the interstitial fluid. We evolve these systems to a dynamic steady state and then measure overall characteristics such as fluid-solid slip velocity, the orientation of the fibers with respect to gravity, and velocity fluctuation levels. These results can be placed in context by e.g. comparing them to results from the literature¹³ for spherical particles. The aim of this paper thus is to characterize the dynamics and structure of dense, homogeneous suspensions of cylindrical particles in liquid through particle-resolved numerical simulation.

The paper is organized as follows: in the next section the flow systems are defined and the main dimensionless numbers characterizing them introduced. We then discuss the numerical method which is an extension of a method we introduced in 2012¹⁴, and provide numerical settings. The subsequent *Results* section begins with qualitative impressions of the flow systems studied and results of verification tests – primarily domain size and spatial resolution effects. Then results in terms of average quantities over the full dimensionless parameter range covered in this paper are discussed. In the final section we reiterate the main conclusions and provide a perspective on future research.

Flow systems

Solid cylindrical particles with length ℓ , diameter d , and density ρ_p are placed in a three-dimensional domain of size $n_x \cdot n_y \cdot n_z$ that contains a Newtonian liquid with density ρ and kinematic viscosity ν . The density ratio has been mostly fixed to $\rho_p/\rho=2.0$ with the exception of one set of simulations where it

was varied between 1.25 and 3. With n identical particles, the overall solids volume fraction is

$$\langle \phi \rangle = \frac{n\pi\ell d^2}{4V} \text{ with } V = nx \cdot ny \cdot nz \text{ the total volume. The flow domain is periodic in all three coordinate}$$

directions. Gravity acts in the negative z -direction, $\mathbf{g} = -g\mathbf{e}_z$. The domain is such that $nx = ny = nz/2$.

Periodicity and the net gravity force on the particles make that it is important to explicitly force-balance the entire solid-fluid system. The procedure we follow in this respect is the same as was described in a previous paper on particle-resolved simulations with *spherical* particles in fully periodic domains.¹³ It is summarized here and – in addition – the consequences for dealing with non-spherical particles are addressed.

The mixture density is defined as $\bar{\rho} \equiv \langle \phi \rangle \rho_p + (1 - \langle \phi \rangle) \rho$. Then the net gravity force on one particle is $\mathbf{F}_g = -(\rho_p - \bar{\rho})V_p g\mathbf{e}_z$ with $V_p = \frac{\pi}{4}\ell d^2$ the volume of the particle. If there are n identical particles, the total downward force is $-(\rho_p - \bar{\rho})nV_p g\mathbf{e}_z = -(1 - \langle \phi \rangle)(\rho_p - \rho)\phi V g\mathbf{e}_z$. This we compensate by applying a body force (force per unit volume) on the fluid volume $(1 - \langle \phi \rangle)V$ in positive z -direction: $\mathbf{f}_b = (\rho_p - \rho)\phi g\mathbf{e}_z$.

The equation of linear motion of a particle is written as

$$V_p \rho_p \frac{d}{dt} \mathbf{u}_p = \mathbf{F}_h + \mathbf{F}_c - (\rho_p - \bar{\rho})V_p g\mathbf{e}_z \quad (1)$$

with \mathbf{F}_h the force the fluid exerts on the particle, and \mathbf{F}_c the contact force due to collisions with other particles and close-range interactions (e.g. lubrication) between particles. The way \mathbf{F}_h and \mathbf{F}_c are determined in a simulation is explained in the next section.

The equation of rotational motion of a particle is¹⁵

$$\mathbf{I} \frac{d}{dt} \boldsymbol{\omega}_p + \boldsymbol{\omega}_p \times (\mathbf{I} \boldsymbol{\omega}_p) = \mathbf{T}_h + \mathbf{T}_c \quad (2)$$

with \mathbf{I} the moment of inertia tensor, and \mathbf{T}_h and \mathbf{T}_c hydrodynamic and contact torque respectively. We will be solving this equation for each particle in a reference frame attached to the particle. Then the moment of inertia tensor is diagonal with $I_{11} = \frac{1}{8} \rho_p V_p d^2$ and $I_{22} = I_{33} = \rho_p V_p \left(\frac{1}{16} d^2 + \frac{1}{12} \ell^2 \right)$ where the “1” direction is along the center line of the cylinder and the “2” and “3” direction are two orthogonal lateral directions. The kinematics of rotation has been dealt with through quaternions. This also will be discussed in the next section.

In dimensionless terms, the physical input parameters of the simulation are aspect ratios (ℓ/d and nx/d , $nx/nz = ny/nz = \frac{1}{2}$), the density ratio $\gamma \equiv \rho_p/\rho$, and the Galileo number $Ga = gd^3/\nu^2$. Galileo number and density ratio can be combined to form the Archimedes number $Ar = Ga(\gamma - 1)$. As an important output parameter we will be considering the Reynolds number based on the slip velocity

between solids and liquid: $Re = \frac{\overline{\langle u_z \rangle - \langle u_{pz} \rangle} d_e}{\nu}$ where $\langle u_z \rangle$ is the volume-averaged superficial velocity in the z -direction, $\langle u_{pz} \rangle$ the average velocity of the particles in z -direction, and the overbar indicates averaging over a time window during which the system is in a dynamically steady state. As the length scale the equivalent particle diameter d_e is introduced. It is the diameter of a sphere that has the same volume as a particle: $d_e = \sqrt[3]{3\ell d^2/2}$. We note that the slip velocity $\overline{\langle u_z \rangle - \langle u_{pz} \rangle}$ is the velocity that would be observed in settling experiments such as the ones reported by Richardson & Zaki^{16,17} and therefore will also be referred to as (average) *settling velocity* in this paper.

Numerical procedures

The simulation procedure consists of (1) a lattice-Boltzmann (LB) solver for the fluid flow; (2) an immersed boundary method to impose no-slip at the particle surfaces; (3) a collision algorithm that detects (near-) contact between particles and determines contact forces and torques (\mathbf{F}_c and \mathbf{T}_c in Eqs. 1

and 2 respectively); (4) an ODE solver that updates particle linear and angular velocities and particle center locations; (5) a quaternion-based procedure for keeping track of particle orientations. For items (1), (2), and (4), the methods are very much the same as the ones used to generate the results in Reference 13 for liquid-fluidized spherical particles. Item (3) (collisions) is different: a hard-spheres, event-driven approach in ¹³ is replaced by a soft-collisions approach in the current paper. There was no need for item (5) in [13] since for spheres there is no need for keeping track of orientation.

The LB scheme we used is due to Somers and Eggels^{18,19}. It uses a uniform, cubic lattice with spacing Δ and takes time steps Δt . It has been supplemented with an immersed boundary method to impose velocities at off-lattice locations through interpolation and forcing.^{20,21,22} The cylindrical surfaces are represented by closely spaced marker points (nearest neighbor distance $\approx 0.5\Delta$). At these points, the fluid is forced to match the solid surface velocity (that can be calculated from the linear and angular velocity of the cylinder) so that no-slip is achieved. By integrating the forces required to impose no-slip over the surface of each particle, the total force and torque each particle exerts on the fluid can be calculated; these we give symbols \mathbf{F}_{ib} and \mathbf{T}_{ib} respectively. This force and torque are exerted on the fluid external to the particle, as well as to the fluid internal to the particle. The latter contributions (\mathbf{F}_{int} and \mathbf{T}_{int}) can be estimated by assuming that the internal fluid moves as a solid body with the particle.^{23,24} The hydrodynamic force and torque (\mathbf{F}_{h} and \mathbf{T}_{h} in Eqs. 1 and 2) on each particle become $\mathbf{F}_{\text{h}} = -(\mathbf{F}_{\text{ib}} - \mathbf{F}_{\text{int}})$ and $\mathbf{T}_{\text{h}} = -(\mathbf{T}_{\text{ib}} - \mathbf{T}_{\text{int}})$ respectively. The dynamical equations for particle linear and angular velocity then can be written as

$$V_p (\rho_p - \rho) \frac{d}{dt} \mathbf{u}_p = -\mathbf{F}_{\text{ib}} + \mathbf{F}_{\text{c}} - (\rho_p - \rho) V_p g \mathbf{e}_z \quad (3)$$

$$(\mathbf{I} - \mathbf{I}_{\text{int}}) \frac{d}{dt} \boldsymbol{\omega}_p + \boldsymbol{\omega}_p \times ((\mathbf{I} - \mathbf{I}_{\text{int}}) \boldsymbol{\omega}_p) = -\mathbf{T}_{\text{ib}} + \mathbf{T}_{\text{c}} \quad (4)$$

In Eq. 4, \mathbf{I}_{int} is the moment of inertia of the internal fluid. For modest to low density ratios the coefficients in front of the d/dt terms of Eqs. 3 and 4 can get small. This then leads to severe time step

limitations if an Euler forward method would be applied to integrate the equations numerically. For this reason, a split-derivative time-stepping procedure^{14,21} has been used for updating Eqs. 3 and 4. This allows a time step that is the same as the time step of the LB scheme. The term

$$V_p (\rho_p - \rho) \frac{d}{dt} \mathbf{u}_p = V_p \rho_p \left(1 - \frac{1}{\gamma} \right) \frac{d}{dt} \mathbf{u}_p \text{ in Eq. 3 has been discretized as } V_p \rho_p \left[\frac{\mathbf{u}_p^{(k+1)} - \mathbf{u}_p^{(k)}}{\Delta t} - \frac{1}{\gamma} \frac{\mathbf{u}_p^{(k)} - \mathbf{u}_p^{(k-1)}}{\Delta t} \right]$$

with (k) denoting the time level. This then leads to the following update rule for linear velocity

$$\mathbf{u}_p^{(k+1)} = \left(1 + \frac{1}{\gamma} \right) \mathbf{u}_p^{(k)} - \frac{1}{\gamma} \mathbf{u}_p^{(k-1)} - \frac{\Delta t \mathbf{F}_{\text{ib}}^{(k)}}{V_p \rho_p} + \frac{\Delta t \mathbf{F}_{\text{c}}^{(k)}}{V_p \rho_p} - \Delta t \left(1 - \frac{1}{\gamma} \right) g \mathbf{e}_z \quad (5)$$

Once linear velocity is updated, we displace the center location of each particle through an Euler explicit step: $\Delta \mathbf{x}_p = \mathbf{u}_p \Delta t$.

Rotational motion of each particle is solved in a reference frame attached to the particle so that the moment of inertia tensor is diagonal and constant. An approach analogous to that of linear motion has been followed for numerically integrating rotational motion (Eq. 4):

$$\boldsymbol{\omega}_p^{(k+1)} = \left(1 + \frac{1}{\gamma} \right) \boldsymbol{\omega}_p^{(k)} - \frac{1}{\gamma} \boldsymbol{\omega}_p^{(k-1)} - \Delta t \mathbf{I}^{-1} \mathbf{T}_{\text{ib}}^{(k)} + \Delta t \mathbf{I}^{-1} \mathbf{T}_{\text{c}}^{(k)} - \Delta t \left(1 - \frac{1}{\gamma} \right) \mathbf{I}^{-1} \left[\boldsymbol{\omega}_p^{(k)} \times (\mathbf{I} \boldsymbol{\omega}_p^{(k)}) \right] \quad (6)$$

Keeping track of the orientation of the particles makes use of quaternions.^{24,25} Each particle's orientation is characterized with a unit quaternion $q = (q_0, \mathbf{q})$ with q_0 a scalar value and \mathbf{q} a three-dimensional vector (q_1, q_2, q_3) and $\sqrt{q_0^2 + q_1^2 + q_2^2 + q_3^2} = 1$. An exact solution for the evolution of a quaternion rotating with an angular velocity $\boldsymbol{\omega}_p$ over a time interval Δt starting from $q^{(k)}$ at time level (k) is available²⁶:

$$q^{(k+1)} = q^{(k)} \circ \left(\cos\left(\frac{1}{2} \Delta t\right), \boldsymbol{\omega}_p \sin\left(\frac{1}{2} \Delta t\right) \right) \quad (7)$$

with the symbol \circ denoting a quaternion multiplication. We use Eq. 7 for updating the quaternion of each particle from one time step to the next.

Quaternions effectively facilitate transferring information between the (x_1, x_2, x_3) coordinate system attached to a cylinder and the inertial (x, y, z) system. The rotation of a vector \mathbf{x} in the (x_1, x_2, x_3) system to a vector \mathbf{y} in the (x, y, z) can be expressed as

$$\mathbf{y} = \mathbf{S}\mathbf{x} \quad (8)$$

with²⁴

$$\mathbf{S} = \begin{bmatrix} 1 - 2(q_2^2 + q_3^2) & 2(q_1q_2 - q_0q_3) & 2(q_1q_3 + q_0q_2) \\ 2(q_2q_1 + q_0q_3) & 1 - 2(q_1^2 + q_3^2) & 2(q_2q_3 - q_0q_1) \\ 2(q_3q_1 - q_0q_2) & 2(q_3q_2 + q_0q_1) & 1 - 2(q_1^2 + q_2^2) \end{bmatrix} \quad (9)$$

The coordinates of the marker points for the IBM are stored for one reference cylinder in the (x_1, x_2, x_3) coordinate system. Equation 8 is used for each cylinder at each time step to transfer its marker points to the (x, y, z) system in order to apply the IBM. One result of the IBM is the torque \mathbf{T}_{ib} associated to each particle in the (x, y, z) system. Since we solve the equation of rotational motion (Eq. 4) in the (x_1, x_2, x_3) system, \mathbf{T}_{ib} needs to be rotated to the latter system. This requires the inverse of \mathbf{S} which is its transpose: $\mathbf{S}^{-1} = \mathbf{S}^T$. As is described below, the matrix \mathbf{S} also is beneficial when performing collisions between particles.

We are dealing with dense suspensions and expect collisions between particles to be frequent. The marker points for executing the IBM are used to detect close proximity between particle surfaces. Below a certain threshold, this proximity then locally activates a repulsive force that performs the collision. Consider two marker points “1” and “2” that belong to two different particles (Particle *A* and Particle *B*), see Figure 1. Each marker point is accompanied by a unit vector that is normal to the particle’s surface, pointing outward. The contact force contribution on Particle *A* due to the proximity of points 1 and 2 is determined as

$$\mathbf{F}_{12} = k(\delta_0 - \delta) \frac{|\delta_\lambda - \lambda|}{\lambda} \frac{(\mathbf{n}_2 - \mathbf{n}_1)}{|\mathbf{n}_2 - \mathbf{n}_1|} \text{ if } \delta < \delta_0 \text{ and } |\delta_\lambda| < \lambda; \quad \mathbf{F}_{12} = \mathbf{0} \text{ otherwise} \quad (10)$$

where we have three model parameters: a spring constant k , a threshold normal distance δ_0 , and a lateral threshold distance λ . The total contact force on Particle A is the sum of all contact forces of all particles surrounding Particle A . For calculating the contribution of \mathbf{F}_{12} to the contact torque on Particle A , we assume \mathbf{F}_{12} to act at Point 1.

It should be noted that the contact force at Point 1 due to Point 2 acts in the direction $(\mathbf{n}_2 - \mathbf{n}_1)$, not in the direction \mathbf{n}_1 normal to the surface of Particle A . In this way the force at Point 2 due to Point 1 is in exactly the opposite direction and of the same magnitude: $\mathbf{F}_{21} = -\mathbf{F}_{12}$.

In DEM simulations, it is usual practice to include damping in the collision process, thereby mimicking a restitution coefficient smaller than one and mitigating instabilities. In particle-resolved simulations, damping is – at least partly – taken care of by resolving the fluid flow in between particle surfaces. When the space between particle surfaces gets smaller than one lattice-spacing, however, the flow there is not sufficiently resolved. For simulations involving resolved spherical particles it is then common practice to add radial lubrication forces based on low-Reynolds analytical expressions²⁷ to the forces acting on the particles.^{13,29} Sometimes also tangential lubrication forces as well as torques are included.²⁸ In this paper the role of lubrication/damping forces has been explored by explicitly including forces that are proportional to the velocity difference between marker points in close proximity. Suppose the two marker points in Figure 1 have velocity \mathbf{u}_1 and \mathbf{u}_2 due to the translational and rotational motion of particle A and B respectively. Their relative velocity is decomposed in the velocity along the average unit normal $\Delta\mathbf{u}^n = (\mathbf{n}_2 - \mathbf{n}_1) \cdot (\mathbf{u}_2 - \mathbf{u}_1) \frac{(\mathbf{n}_2 - \mathbf{n}_1)}{|\mathbf{n}_2 - \mathbf{n}_1|}$ and the velocity perpendicular to the average unit normal $\Delta\mathbf{u}^t = (\mathbf{u}_2 - \mathbf{u}_1) - \Delta\mathbf{u}^n$. The normal and tangential damping force are written as

$$\mathbf{F}_{12}^n = k^n \left(\frac{1}{\delta^*} - \frac{1}{\delta_d} \right) \frac{|\delta_\lambda - \lambda|}{\lambda} \Delta\mathbf{u}^n \quad \text{if } \delta^* < \delta_d \text{ and } |\delta_\lambda| < \lambda; \quad \mathbf{F}_{12}^n = \mathbf{0} \text{ otherwise} \quad (11)$$

$$\mathbf{F}_{12}^t = k' \left(\frac{1}{\delta^*} - \frac{1}{\delta_d} \right) \frac{|\delta_\lambda - \lambda|}{\lambda} \Delta \mathbf{u}^t \quad \text{if } \delta^* < \delta_d \text{ and } |\delta_\lambda| < \lambda; \quad \mathbf{F}_{12}^t = \mathbf{0} \text{ otherwise} \quad (12)$$

with

$$\delta^* = \delta \text{ if } \delta > \delta_{sat} \text{ and } \delta^* = \delta_{sat} \text{ if } \delta \leq \delta_{sat} \quad (13)$$

Here we – again – introduce a number of parameters. The pre-factors k^n and k' determine the strength of the damping interactions; δ_d is the distance along the average normal of two marker points below which the damping force becomes active; δ_{sat} is the distance below which the damping force saturates.

The $\left(\frac{1}{\delta^*} - \frac{1}{\delta_d} \right)$ dependence is borrowed from expressions for the radial lubrication force between spherical particles in particle-resolved simulations.²⁸ The parameter δ_d then depends on the spacing of the grid on which the fluid flow is solved. If the distance between particle surfaces is larger than δ_d , the flow between the surfaces is considered resolved and no additional lubrication force is required; if the distance becomes smaller than δ_d , the lubrication force is switched on. In this paper we set $\delta_d = \Delta$. Given that the lubrication force diverges for $\delta \rightarrow 0$ it has been saturated below a certain threshold distance (δ_{sat}).¹³ In a numerical sense we want to avoid large damping forces, in a physical sense saturation occurs as a result of surface roughness.

For spherical particles, tangential lubrication follows a $\ln \delta$ rather than a $1/\delta$ relationship. Here, for simplicity, tangential lubrication and normal lubrication are given similar expressions. By setting $k' = 0.1k^n$ it is ensured that tangential lubrication is weaker by an order of magnitude than normal lubrication, something we observed in simulations with spherical particles.¹³ The parameter k^n is treated as an ad-hoc parameter. It will require future refinements as it – in principle – depends on the fluid viscosity as well on the shape (local curvature) of the solid surfaces in close proximity. Specific values for the model parameters are given and motivated in the next section.

Set-up of simulations

Particles are placed in a non-overlapping manner in the $nx \cdot ny \cdot nz$ fully periodic flow domain. Initially fluid and particles are at rest. At time zero, gravity and the body force on the liquid \mathbf{f}_b become active and we let the system develop to a dynamically steady state. This process we monitor by keeping track of

$\text{Re} = \frac{|\langle u_z \rangle - \langle u_{pz} \rangle| d_e}{\nu}$ as a function of time. After reaching dynamically steady state, the simulations are

continued in order to collect data for determining statistical flow quantities. The length of this averaging time window is of the order of $10d^2/\nu$. All average flow quantities reported were based on data collected in steady-state time windows.

As for the choice of numerical parameters, the most important one is the spatial resolution of a simulation. Since we use uniform cubic lattices it can be expressed as the number of lattice distances Δ spanning the diameter d of a cylinder. The default resolution is $d = 16\Delta$ and resolution effects have been studied by also simulating systems with $d = 12\Delta$ and $d = 24\Delta$. The default domain size is $nx \cdot ny \cdot nz = 9d \cdot 9d \cdot 18d$.

We want the collisions as much as possible to happen when cylinder surfaces actually touch, i.e. not before surfaces touch and not when cylinder volumes overlap. In the former scenario the particles are behaving as slightly larger, in the latter as slightly smaller than they actually are which has consequences for the effective solids volume fraction and thus potentially for slip velocities. Previous work¹⁴ shows that if the spring constant $k \approx 0.2\rho_p V_p |\mathbf{u}_p|^2 / \delta_0^2$ (Eq. 10), surfaces approximately touch at the moment their relative velocity is reverted in a collision. The simulations are designed such that particle speeds $|\mathbf{u}_p|$ are of the order 10^{-2} in lattice units. We chose the interaction distance (see Eq. 10) $\delta_0 = 0.02d$. This then sets k to a value of the order of 5.

The lubrication coefficient k^n is estimated in analogy with spherical particles of diameter d . For such systems the pre-factor in Eq. 11 would read $k^n = 3\pi\rho\nu d^2/8$; this expression we apply for cylindrical

particles having diameter d . As mentioned above, $k^t = 0.1k^n$ and $\delta_d = \Delta$. Finally, the lubrication saturation distance has been set to $\delta_{sat} = 0.1\Delta$.

Results

Effects of numerical settings and domain size

First it will be established to what extent numerical settings impact the behavior of the two-phase flow systems being investigated. In order to accommodate fine meshes, spatial resolution effects were tested in relatively small domains with size $nx \cdot ny \cdot nz = 6d \cdot 6d \cdot 12d$ (i.e. smaller than the default size by a factor $2/3$ in each coordinate direction). In Figure 2, results for two particle types ($\ell/d = 1$ and $\ell/d = 2$), achieved on three grids (with particle diameter over grid spacing $d/\Delta = 12, 16$ and 24) are compared in terms of the Reynolds number based on the average slip velocity Re , as well as in terms of the Reynolds number based on the particles' fluctuating velocities $Re_{rms,\alpha} = d_e \sqrt{\langle (u_{p\alpha} - \langle u_{p\alpha} \rangle)^2 \rangle} / \nu$, with α a coordinate direction (z is vertical, xy is horizontal). In addition to spatial resolution effects, also the impact of the kinematic viscosity of the liquid (in lattice units) has been assessed. Lattice-Boltzmann simulations of suspensions of spherical particles using the immersed boundary method showed – at fixed Reynolds numbers – some effect of viscosity on the drag force.²² All results in Figure 2 are for the same Galileo number of $Ga=864$; at given diameter and viscosity, gravitational acceleration was adapted to achieve this value.

Viscosity effects are most pronounced for the lower resolution of $d/\Delta = 12$ and reduce quickly on finer grids. For a viscosity $\nu = 0.02$ (in lattice units) the resulting Reynolds numbers depend strongest on the resolution, for instance showing an increase of 7% in the slip-velocity Reynolds number of $\ell/d = 2$ cylinders when refining from $d/\Delta = 12$ to 24 . The higher viscosities have much weaker dependencies on resolution. Slip velocity Reynolds number variations are within 2%. Based on these observations and

considering computational feasibility, the results presented in the remainder of this paper are with a resolution of $d/\Delta = 16$ and kinematic viscosities of $\nu = 0.04$ or 0.06 .

By applying fully periodic boundary conditions, we attempt to represent an unconfined flow and so mimic what is happening in a fluidized system away from walls or other obstructions. In principle, particles and fluid interact with themselves over the periodic boundaries so that we need sufficiently large domains for representative simulations. In Figures 3 (qualitative) and 4 (quantitative) we compare results obtained with different domain sizes. From Figure 4 we conclude that Reynolds numbers based on the average slip velocity (Re) are quite insensitive for the system size. In the range $nx/d = 6 - 12$ differences are less than 3% with slightly increasing slip velocities for larger domains; the strongest sensitivity is for the largest ($\ell/d = 4$) cylinders.

The Reynolds numbers associated with the fluctuating particle velocities clearly depend on domain size. Where for the smallest cylinders considered ($\ell/d = 1$) we might see convergence when extending the domain from $nx/d = 9$ to 12, this is not the case for the longer cylinders where differences of up to 15% are observed.

For reasons of computational affordability, this paper will mainly present results obtained in domains with $nx/d = 9$ for which average slip velocities have largely converged, and fluctuating velocities – admittedly – have not. Impressions of simulations in such domains are given in Figure 5 for the four cylinder aspect ratios. In the cases shown in the figure, and also in other cases, the distribution of particles is more or less homogeneous over the domain volume. We have not observed the voidage wave instabilities that have been reported – experimentally as well as computationally – in liquid fluidized beds with uniformly sized spherical particles.^{13,28}

Average flow quantities at constant Ga

A series of simulations have been conducted to study hindered settling as a function of solids volume fraction and cylinder aspect ratio at a constant Galileo number of $Ga=864$. In experimental terms this means that we fluidize cylinders of the same diameter d with different lengths and in different quantities

made of the same solid material in the same liquid feeling the same gravitational acceleration. Under the earth's gravity and with $d=1$ mm cylinders, $Ga=864$ would be achieved in a liquid with kinematic viscosity of $\nu \approx 3.4 \cdot 10^{-6}$ m²/s. The density ratio was $\gamma = 2.0$.

Results for average settling velocities are presented in Figure 6 in a double-logarithmic form that anticipates a Richardson & Zaki relation^{16,30} to describe hindered settling: $Re = Re_{\infty} (1 - \langle \phi \rangle)^N$. As can be seen, this relation represents the results well and allows – through least-squares fitting – for determination of the parameters Re_{∞} and N . Clearly Re_{∞} increases with increasing ℓ/d , simply because the particles get larger. There also is a consistent trend of N with ℓ/d with N reducing from 4.34 to 3.32 if ℓ/d increases from 0.5 to 4.0.

It is hypothesized that the variation in the exponent N with ℓ/d as observed in Figure 6 is related to the way the particles orient themselves and/or the levels with which their velocities fluctuate. We first note, however, that for spherical particles it was already asserted by Richardson & Zaki¹⁶ that the exponent N depends on the Reynolds number:

$$N = 4.45 Re_{\infty}^{-0.1} \quad \text{for } 1 < Re_{\infty} < 500 \quad (14)$$

Substituting values of Re_{∞} as derived from the fits in Figure 6 in Eq. 14 results in lower values for N than the ones we obtain for the cylinders (in Figure 6). The extent to which N varies with Re_{∞} according to Eq. 14, however, is of a comparable level as the variations in N found in Figure 6.

The distributions of the angles φ of the cylinders' center lines with the vertical are given in Figure 7 for all the simulations represented in Figure 6. For a randomly oriented collection of cylinders, the end points of cylinders would be uniformly distributed over a sphere with radius $\ell/2$ so that φ is distributed according to $\sin \varphi$ ($0 \leq \varphi \leq \pi/2$); $\varphi = 0$ is vertical orientation; $\varphi = \pi/2$ horizontal. The cylinders with $\ell/d = 1$ closely follow this $\sin \varphi$ behavior for all solids volume fractions. Only for the highest ($\langle \phi \rangle = 0.48$) there is a slight preference for horizontal orientations. Particles with $\ell/d = 0.5$ are disks.

Beyond a certain Reynolds number ($Re \approx 7$), single disks tend to orient themselves with their center line vertically.³¹ This then explains the angle distribution for $\langle \phi \rangle = 0.10$ that is skewed towards low values of ϕ . It has $Re \approx 8.7$, as well as sufficient space between the particles to orient themselves as single disks would. Increasing $\langle \phi \rangle$ reduces the Reynolds number as well as the maneuvering space for the particles which leads to a gradual increase in preference for larger angles.

“Long” cylinders ($\ell/d = 4$) orient mostly vertically, at least if $\langle \phi \rangle > 0.10$. This also is qualitatively visible in Figure 5 (right panel). For settling cylinders with higher aspect ratios ($\ell/d \geq 5$) this has been observed experimentally as well.⁷ The cylinders with $\ell/d = 2$ go through an interesting transition with increasing $\langle \phi \rangle$: from a preference for horizontal center lines at low $\langle \phi \rangle$, to more vertical at high $\langle \phi \rangle$; it is the opposite of the transition the $\ell/d = 0.5$ particles go through.

So far, average velocity has been discussed. Particle velocities fluctuate as a result of the random nature of the suspension with – for individual particles – a constantly changing hydrodynamic environment. Particle fluctuations and their scaling with solids volume fraction and Reynolds number are subject of fundamental research³² and are practically relevant for transport processes in multiphase systems as they relate to mixing and dispersion in the solids as well as in the liquid phase.³³ In fluidized systems, particle velocity fluctuations are anisotropic with vertical fluctuations stronger by approximately a factor of 2 compared to horizontal fluctuations.³⁴

Figure 8 shows particle velocity distribution functions confirming the anisotropy in our suspensions: wider distributions for z -velocities compared to xy -velocities. We also see that the width of the distributions very strongly depends on the solids volume fraction: the strong hindrance in dense suspensions limits particle velocity fluctuation levels.

It is usual practice⁷ to normalize particle velocity fluctuation root-mean-square values by the average settling velocity. The way these relative velocity fluctuations depend on solids volume fraction and cylinder aspect ratio is shown in Figure 9. Vertical as well as horizontal component go through a

maximum at $\langle \phi \rangle \approx 0.3$, irrespective of ℓ/d . Similar profiles have been reported experimentally as well as computationally for spherical particles at low³⁴ as well as intermediate³³ Reynolds numbers. In addition, a clear trend with respect to ℓ/d can be observed: the lower aspect ratios have higher relative velocity fluctuation levels.

Average flow quantities at constant Galileo number based on equivalent diameter

We thus observe significant differences in the behavior and structure of the suspension with aspect ratio ℓ/d and overall solids volume fraction $\langle \phi \rangle$. Since the Reynolds numbers changed as ℓ/d changed, it is worthwhile to clarify to what extent the differences observed can be ascribed to ℓ/d and/or to Re.

Aspect ratio and Reynolds number can be decoupled by scaling the flow systems differently. So far we kept $Ga = gd^3/\nu^2$ constant, motivated by considerations for experimental validation (comparing cylinders with the same diameter but different lengths). If instead, we keep $Ga_e = gd_e^3/\nu^2$ constant, we are comparing cylinders of different length having the same volume, that will show – at the same $\langle \phi \rangle$ – comparable average settling speeds and thus Reynolds numbers. We have set $Ga_e = 1.5 \cdot 864 = 1296$ and performed a series of simulations varying ℓ/d and $\langle \phi \rangle$ in the same range as in the previous section, keeping the density ratio constant at $\gamma = 2$. In these simulations, Ga_e has been kept constant by appropriately setting g . For the chosen value of $Ga_e = 1296$, the systems with $\ell/d = 1$ in this section are the same as the ones with $Ga = 864$ in the previous section.

The hindered settling behavior is shown in Figure 10. It is remarkable to see that now the results for the different cylinder aspect ratios almost collapse, i.e. the settling velocity Reynolds number primarily depends on the solids volume fraction, and hardly on ℓ/d . For further interpretation, the data are also plotted on a linear Reynolds number scale in Figure 10, leading to the same conclusion. The “universal” Richardson & Zaki exponent is to a good approximation the one that was found for $\ell/d = 1$ in Figure 6: $N \approx 3.9$. Qualitatively, the orientation angle distributions remain unaltered as compared to the set

obtained for $Ga = 864$ (Figure 7), see Figure 11 (where we omitted the $\ell/d = 1$ distributions as they are the same as in Figure 7). The most striking difference between the angle distributions in Figure 11 and in Figure 7 is the more pronounced vertical alignment of the cylinders with $\ell/d = 4$ at the higher solids volume fractions in Figure 7, i.e. the alignment slightly reduces when the Reynolds number gets smaller.

Relative particle velocity fluctuation levels are shown in Figure 12. The overall trend is the same as for the previous set of simulations: highest levels at $\langle \phi \rangle \approx 0.3$ and vertical velocity fluctuations approximately a factor of two larger than horizontal velocity fluctuations. Closer comparison between Figure 9 ($Ga = 864$) and Figure 12 ($Ga_e = 1296$) shows a weaker sensitivity of relative fluctuation levels with respect to ℓ/d . Where in Figure 9 the clear trend is a decrease of fluctuation levels with increasing ℓ/d , this is much less so in Figure 12, although also there the $\ell = 4d$ particles have the weakest fluctuations.

In a final set of simulations we consider the role of the Archimedes number (based on the equivalent diameter d_e): $Ar_e = (\gamma - 1)gd_e^3/\nu^2 = (\gamma - 1)Ga_e$. Above, $Ga_e = 1296$ and $\gamma = 2$ were constant so that Ar_e is constant. We now keep Ar_e constant at $Ar_e = 1296$ and vary the density ratio in such a way that the net weight of a single particle (proportional to $(\gamma - 1)gd_e^3$) is the same for all aspect ratios; Ga_e is thus not constant anymore. The results of this set of simulations are compared to the ones with $Ga_e = 1296$ in Table 1 in terms of average settling velocity Reynolds number and relative particle velocity fluctuation levels. There is a close agreement between the two sets of simulations from which we conclude that – under the conditions investigated – the density ratio has limited significance for these average flow properties.

Conclusions

This paper reports on particle-resolved simulations of dense suspensions of cylindrical solid particles in Newtonian liquid. Fully periodic, three-dimensional domains were used to study fluidization / hindered

settling of cylinders that varied in length-over-diameter aspect ratio from 0.5 to 4. We demonstrated that it was feasible to choose the simulation parameters such that grid-independent results for average and fluctuating velocities could be obtained. Fluctuating velocity levels increased with the size of the periodic computational domains to an extent that was different for different aspect ratios. Therefore, results for these quantities are likely underestimated in the current study. Average velocities were to a good approximation independent of domain size.

We observed significant differences in the way the particles are oriented relative to the vertical (gravity) direction. The orientations of cylinders with aspect ratio 1 are randomly oriented, almost irrespective of the solids volume fraction. The longer cylinders – specifically those with aspect ratio 4 – orient themselves preferentially vertically. For the other aspect ratios a significant dependency on the solids volume fraction of the distributions of orientation angles is observed.

It is striking to see that the hindered settling behavior, i.e. the way the Reynolds number based on average settling velocity and equivalent diameters depends on the solids volume fraction, is almost independent of the aspect ratio of the cylinders if the Archimedes number based on the equivalent diameter is kept constant. This despite the fact that the orientation of the cylinders does depend on aspect ratio. As for spherical particles, the Richardson & Zaki exponent (N) depends on the Reynolds number.

There is a clear need for experimental validation of the results presented here. Experiments are – among more – needed to provide guidance for establishing parameters related to short-range interactions that in this paper have been treated in an ad-hoc manner without much regard for the details of lubrication flow in the narrow (in the simulations unresolved) space between particles. By performing sensitivity analyses and comparing results with detailed (refractive index matched) quantitative flow visualizations, the importance of modeling short range interaction can be assessed and modeling can be improved.

The computational demands of the simulations presented here are still fairly modest. All results presented are based on sequential simulations, requiring of the order of 3 Gbyte of memory and running 5

to 10 days for equilibration and collection of data for statistical analysis. Parallelization of the computer code for simulating larger domains with more particles is an important step to take in future work.

References

- [1] Kidanemariam AG, Uhlmann M. Formation of sediment patterns in channel flow: minimal unstable systems and their temporal evolution. *J. Fluid Mech.* 2017; 818: 716–743.
- [2] Rubinstein GJ, Derksen JJ, Sundaresan S. Lattice-Boltzmann simulations of low-Reynolds number flow past fluidized spheres: effect of Stokes number on drag force. *J. Fluid Mech.* 2016; 788: 576–601.
- [3] Capecelatro J, Desjardins O. An Euler–Lagrange strategy for simulating particle-laden flow., *J. Comp. Phys.* 2013; 238: 1–31.
- [4] Derksen JJ. Eulerian-Lagrangian simulations of settling and agitated dense solid-liquid suspensions – achieving grid convergence. *AIChE J.* 2018; 64: 1147–1158.
- [5] Jackson R. *Dynamics of Fluidized particles.* Cambridge: Cambridge University Press, 2000.
- [6] Igci Y, Sundaresan S. Constitutive models for filtered two-fluid models of fluidized gas-particle flows. *Ind. Eng. Chem. Res.* 2011; 50: 13190–13201.
- [7] Hertzhaft B, Guazzelli E. Experimental study of the sedimentation of dilute and semi-dilute suspensions of fibres. *J. Fluid Mech.* 1999; 384: 133–158.
- [8] Salmela J, Martinez DM, Kataja M. Settling of dilute and semidilute fiber suspensions at finite Re. *AIChE J.* 2007; 53: 1916–1923.
- [9] Gustavsson K, Tornberg A-K. Gravity induced sedimentation of slender fibers. *Phys. Fluids* 2009; 21: 123301-1–15.
- [10] Mahajan VV, Nijssen TMJ, Kuipers JAM, Padding JT. Non-spherical particles in a pseudo-2D fluidised bed: Modelling study. *Chem. Eng. Sc.* 2018; 192: 1105–1123.
- [11] Dorai F, Moura Teixeira C, Rolland M, Climent E, Marcoux M, Wachs A. Fully resolved simulations of the flow through a packed bed of cylinders: Effect of size distribution. *Chem. Eng. Sc.* 2015; 129: 180–192.
- [12] Sanjeevi SKP, Kuipers JAM, Padding JT. Drag, lift and torque correlations for non-spherical particles from Stokes limit to high Reynolds numbers. *Int. J. Multiphase Flow* 2018; 106: 325–337.
- [13] Derksen JJ, Sundaresan S. Direct numerical simulations of dense suspensions: wave instabilities in liquid-fluidized beds. *J. Fluid Mech.* 2007; 587: 303–336.
- [14] Shardt O, Derksen JJ. Direct simulations of dense suspensions of non-spherical particles. *Int. J. Multiphase Flow* 2012; 47: 25–36.
- [15] Goldstein H. *Classical mechanics (second edition).* Reading, Massachusetts: Addison-Wesley, 1980.

- [16] Richardson JF, Zaki WN. Sedimentation and fluidisation. Part 1. *Trans. Inst. Chem. Engrs.* 1954; 32: 35–53.
- [17] Derksen JJ. Assessing Eulerian-Lagrangian simulations of dense solid-liquid suspensions settling under gravity. *Comp. & Fluids* 2018; 176: 266–275.
- [18] Somers JA. Direct simulation of fluid flow with cellular automata and the lattice-Boltzmann equation. *App. Sci. Res.* 1993;51: 127–133.
- [19] Eggels JGM, Somers JA. Numerical simulation of free convective flow using the lattice-Boltzmann scheme. *Int. J. Heat Fluid Flow* 1995; 16: 357–364.
- [20] Derksen J, Van den Akker HEA. Large-eddy simulations on the flow driven by a Rushton turbine. *AIChE J.* 1999; 45: 209–221.
- [21] Feng ZG, Michaelides E. Robust treatment of no-slip boundary condition and velocity updating for the lattice-Boltzmann simulation of particulate flows. *Comp. & Fluids* 2009; 38: 370–381.
- [22] Ten Cate A, Nieuwstad CH, Derksen JJ, Van den Akker HEA. PIV experiments and lattice-Boltzmann simulations on a single sphere settling under gravity. *Phys. Fluids* 2002; 14: 4012–4025.
- [23] Uhlmann M. An immersed boundary method with direct forcing for the simulation of particulate flows. *J. Comput. Phys.* 2005; 209: 448–76.
- [24] Suzuki K, Inamuro T. Effect of internal mass in the simulation of a moving body by the immersed boundary method. *Comp. & Fluids* 2011; 49: 173–187.
- [25] Kuipers JB. *Quaternions and Rotation Sequences*. Princeton: Princeton University Press; 1999.
- [26] Phillips WF. Review of attitude representation used for aircraft kinematics. *J. Aircraft* 2001; 38: 718–737.
- [27] Kim S, Karrila SJ. *Microhydrodynamics: Principles and selected applications*. Boston: Butterworth-Heinemann, 1991.
- [28] Nguyen N-Q, Ladd AJC. Lubrication corrections for lattice-Boltzmann simulations of particle suspensions. *Phys. Rev. E* 2002; 66: 046708.
- [29] Duru P, Nicolas M, Hinch J, Guazzelli E. Constitutive laws in liquid-fluidized beds. *J. Fluid Mech.* 2002; 452: 371–404.
- [30] Di Felice R. The voidage function for fluid-particle interaction systems. *Int. J. Multiphase Flow* 1994; 20: 153–159.
- [31] Becker HA. The effects of shape and Reynolds number on drag in the motion of a freely oriented body in an infinite fluid. *Can. J. Chem. Eng.* 1959; 37: 85–91.
- [32] Guazzelli É, Hinch J. Fluctuations and instability in sedimentation. *Annu. Rev. Fluid Mech.* 2011; 43: 97–116.

- [33] Derksen JJ. Simulations of scalar dispersion in fluidized solid-liquid suspensions. *AIChE J.* 2014; 60: 1880–1890.
- [34] Nicolai H, Herzhaft B, Hinch EJ, Oger L, Guazzelli E. Particle velocity fluctuations and hydrodynamic self-diffusion of sedimenting non-Brownian spheres. *Phys. Fluids* 1995; 7: 12–23.

Figure captions

Figure 1. Collision detection between particles A and B that have marker points 1 and 2 and associated outward normals on their surface. An algorithm keeps track of the proximity of marker points on different particles and determines – below a certain threshold – their normal and tangential spacing (δ and δ_λ respectively) Along with the relative velocity of the marker points, this determines the contribution of the contact force on A and B as a result of the proximity of 1 and 2 (Eqs. 10, 11 and 12).

Figure 2. Effect of spatial resolution. Top: average slip-velocity Reynolds number Re as a function of spatial resolution in terms of d/Δ . Bottom: Reynolds numbers associated to the fluctuating velocity Re_{rms} of the particles in vertical (z) and horizontal (xy) direction. Two types of cylinders ($\ell = d$ and $\ell = 2d$) and three kinematic viscosities ν (in lattice units) as indicated. System size $nx/d = 6.0$; $Ga=864$; overall solids volume fraction $\langle\phi\rangle = 0.29$; density ratio $\gamma = 2.0$.

Figure 3. Instantaneous realizations for $\ell = 2d$, $Ga=864$, $\langle\phi\rangle = 0.29$, $\nu=0.04$ (lattice units), and $d/\Delta=16$. From left to right the system size is such that $nx/d = 6, 9, 12$ respectively. The fourth (far right) panel is the same realization as the third panel but now with the particles in front of the fluid velocity contour plane made invisible.

Figure 4. System size effects. Top: average slip-velocity Reynolds number Re as a function of system size nx/d . Bottom: Reynolds numbers associated to the fluctuating velocity Re_{rms} of the particles in vertical (z) and horizontal (xy) direction. Three types of cylinders ($\ell = d$, $\ell = 2d$, $\ell = 4d$) as indicated. $Ga=864$, $\langle\phi\rangle = 0.29$, $d/\Delta=16$, $\nu=0.04$ (lattice units).

Figure 5. Impressions of systems with $Ga=864$, $\langle\phi\rangle = 0.29$, $nx/d=9$, $d/\Delta=16$, $\nu=0.04$ (lattice units) and (from left to right) $\ell/d = 0.5, 1, 2, 4$.

Figure 6. Hindered settling. Slip velocity Reynolds number as a function of $1-\langle\phi\rangle$ for various ℓ/d as indicated. The straight lines are least squares fits according to $Re = Re_\infty (1-\langle\phi\rangle)^N$. $Ga=864$, $nx/d=9$, $d/\Delta=16$, $\nu=0.04$ (lattice units).

Figure 7. Distributions of the angles φ between cylinder centerlines and the vertical for all 20 cases represented in Figure 6 on hindered settling. The drawn black curve in each panel is $\sin\varphi$ which is representative for a random orientation distribution.

Figure 8. Particle velocity distribution functions. Top: $\ell/d=2$; bottom: $\ell/d=4$. The left panels show a comparison between horizontal (xy) and vertical (z) velocities at $\langle\phi\rangle=0.29$. The right panels show a comparison between vertical particle velocity distributions for various $\langle\phi\rangle$.

Figure 9. Particle velocity fluctuation levels $u'_{p\alpha} = \sqrt{\langle(u_{p\alpha} - \langle u_{p\alpha} \rangle)^2\rangle}$ normalized by the average settling velocity $u_{stl} = \left| \langle u_z \rangle - \langle u_{pz} \rangle \right|$ as a function of solids volume fraction for all cases considered in Figure 6 (on hindered settling). Red symbols indicate vertical (z) velocity fluctuations, black symbols horizontal (xy) fluctuations.

Figure 10. Hindered settling. Slip velocity Reynolds number as a function of $1-\langle\phi\rangle$ for various ℓ/d as indicated. Different from Figure 6, now all simulations have the same Galilei number based on the equivalent diameter: $Ga_e=1296$. Top and bottom panel have the same data on a logarithmic and linear Re scale respectively. $nx/d=9$, $d/\Delta=16$, $\nu=0.04$ (lattice units) for $\langle\phi\rangle \leq 0.40$ and $\nu=0.06$ for $\langle\phi\rangle > 0.40$.

Figure 11. Distributions of the angles φ between cylinder centerlines and the vertical for all 20 cases represented in Figure 10 on hindered settling that all have $Ga_e=1296$. The drawn black curve in each panel is $\sin\varphi$ which is representative for a random orientation distribution.

Figure 12. Particle velocity fluctuation levels $u'_{p\alpha} = \sqrt{\langle(u_{p\alpha} - \langle u_{p\alpha} \rangle)^2\rangle}$ normalized by the average settling velocity $u_{stl} = \left| \langle u_z \rangle - \langle u_{pz} \rangle \right|$ as a function of solids volume fraction for all cases considered in Figure 10 with $Ga_e=1296$. Red symbols indicate vertical (z) velocity fluctuations, black symbols horizontal (xy) fluctuations.

Figures

Figure 1. Collision detection between particles A and B that have marker points 1 and 2 and associated outward normals on their surface. An algorithm keeps track of the proximity of marker points on different particles and determines – below a certain threshold – their normal and tangential spacing (δ and δ_λ respectively) Along with the relative velocity of the marker points, this determines the contribution of the contact force on A and B as a result of the proximity of 1 and 2 (Eqs. 10, 11 and 12).

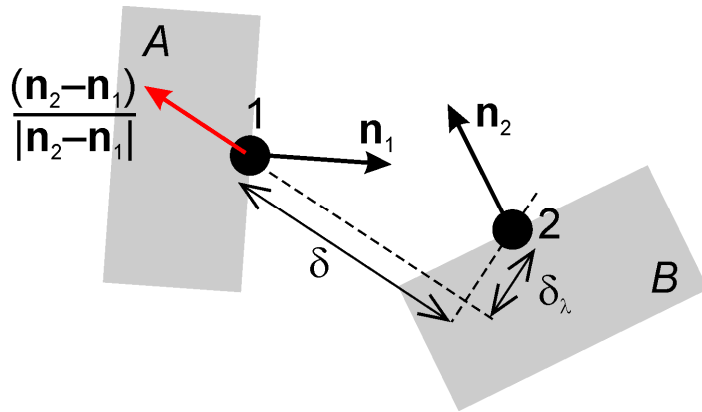


Figure 2. Effect of spatial resolution. Top: average slip-velocity Reynolds number Re as a function of spatial resolution in terms of d/Δ . Bottom: Reynolds numbers associated to the fluctuating velocity Re_{rms} of the particles in vertical (z) and horizontal (xy) direction. Two types of cylinders ($\ell = d$ and $\ell = 2d$) and three kinematic viscosities ν (in lattice units) as indicated. System size $nx/d = 6.0$; $Ga = 864$; overall solids volume fraction $\langle \phi \rangle = 0.29$; density ratio $\gamma = 2.0$.

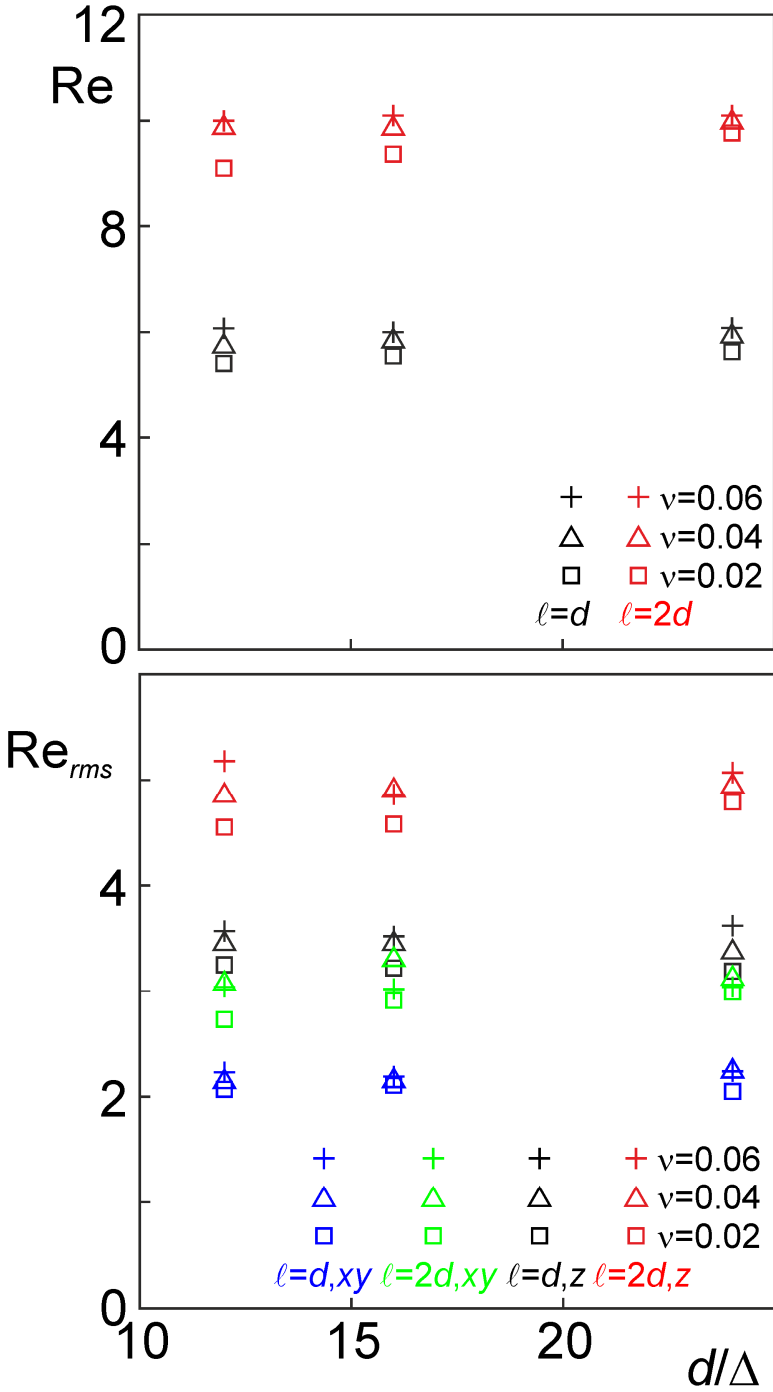


Figure 3. Instantaneous realizations for $\ell = 2d$, $\text{Ga}=864$, $\langle\phi\rangle=0.29$, $\nu=0.04$ (lattice units), and $d/\Delta=16$. From left to right the system size is such that $nx/d = 6, 9, 12$ respectively. The fourth (far right) panel is the same realization as the third panel but now with the particles in front of the fluid velocity contour plane made invisible.

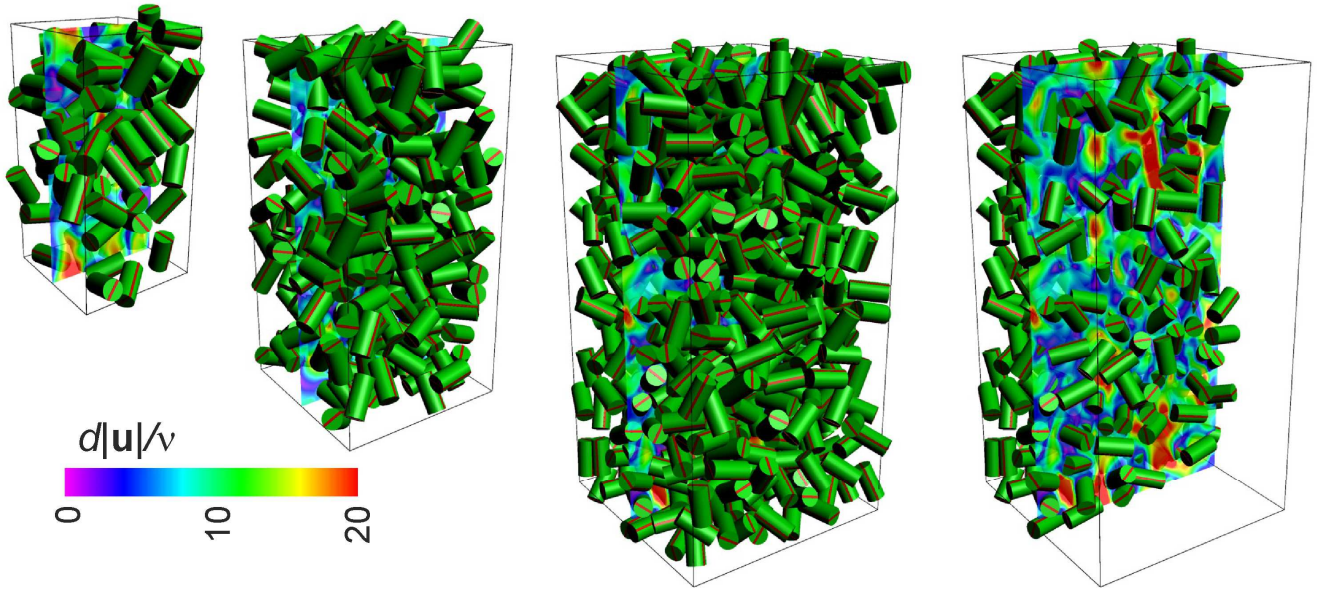


Figure 4. System size effects. Top: average slip-velocity Reynolds number Re as a function of system size nx/d . Bottom: Reynolds numbers associated to the fluctuating velocity Re_{rms} of the particles in vertical (z) and horizontal (xy) direction. Three types of cylinders ($\ell = d$, $\ell = 2d$, $\ell = 4d$) as indicated. $Ga=864$, $\langle\phi\rangle=0.29$, $d/\Delta=16$, $\nu=0.04$ (lattice units).

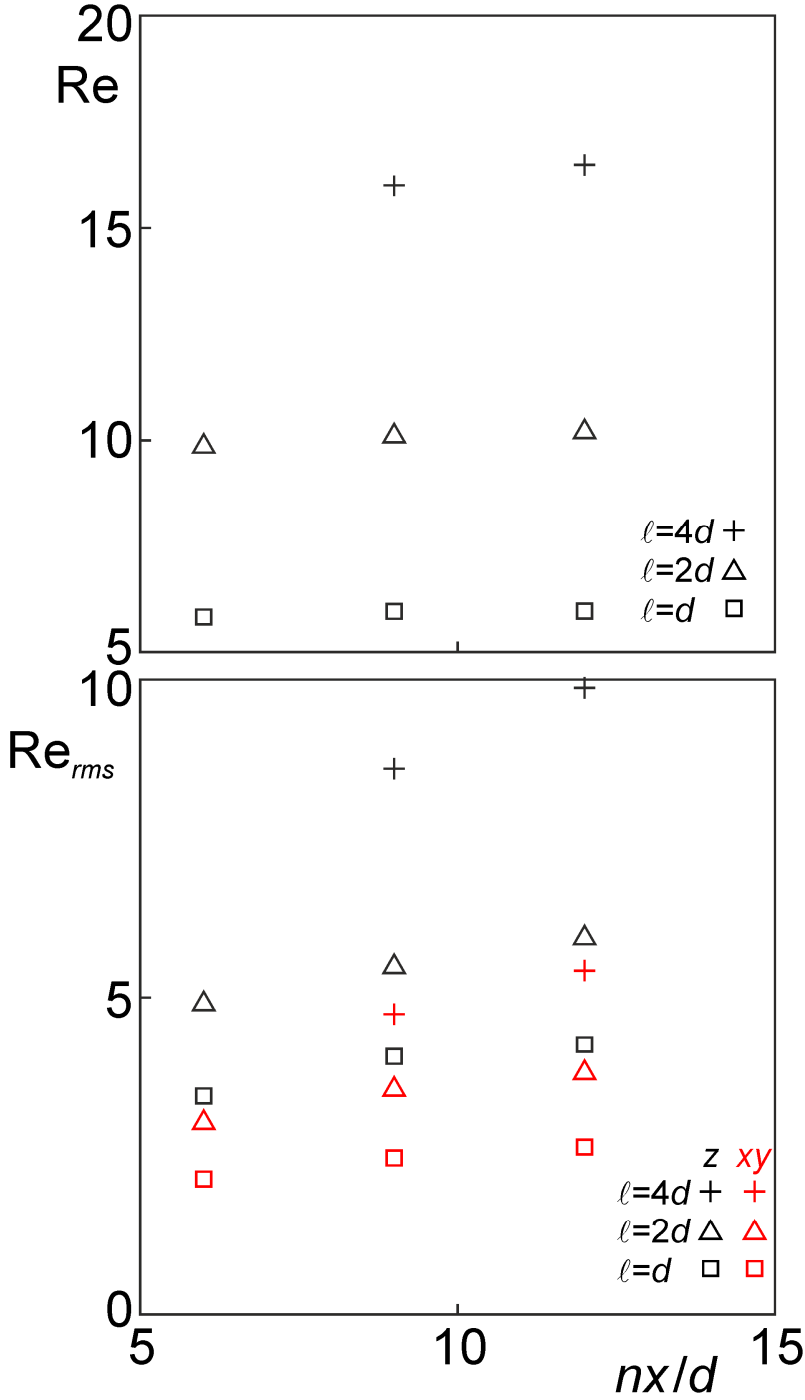


Figure 5. Impressions of systems with $Ga=864$, $\langle\phi\rangle=0.29$, $nx/d=9$, $d/\Delta=16$, $\nu=0.04$ (lattice units) and (from left to right) $\ell/d=0.5, 1, 2, 4$.

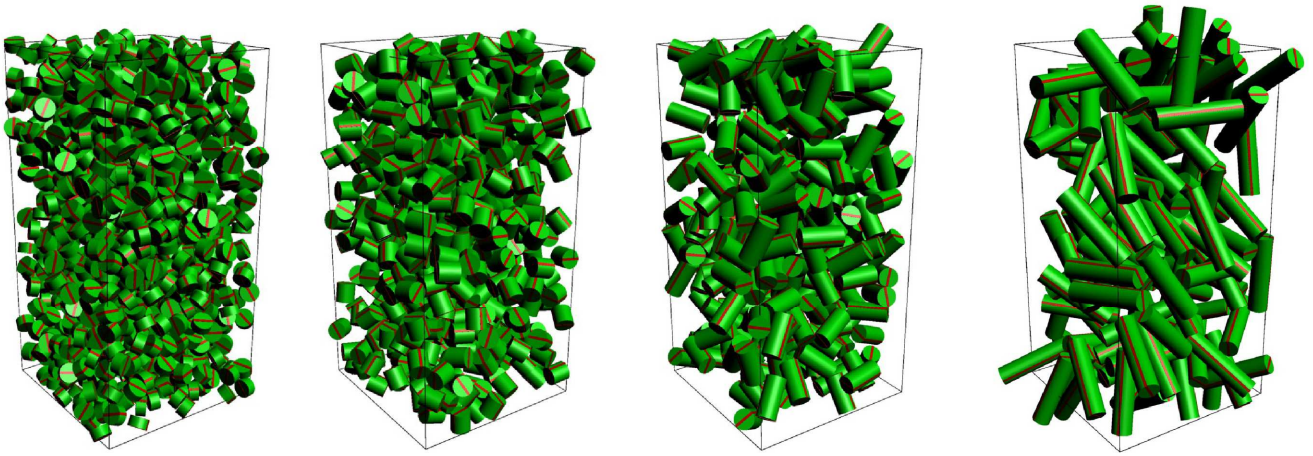


Figure 6. Hindered settling. Slip velocity Reynolds number as a function of $1-\langle\phi\rangle$ for various ℓ/d as indicated. The straight lines are least squares fits according to $Re = Re_\infty(1-\langle\phi\rangle)^N$. $Ga=864$, $nx/d=9$, $d/\Delta=16$, $\nu=0.04$ (lattice units).

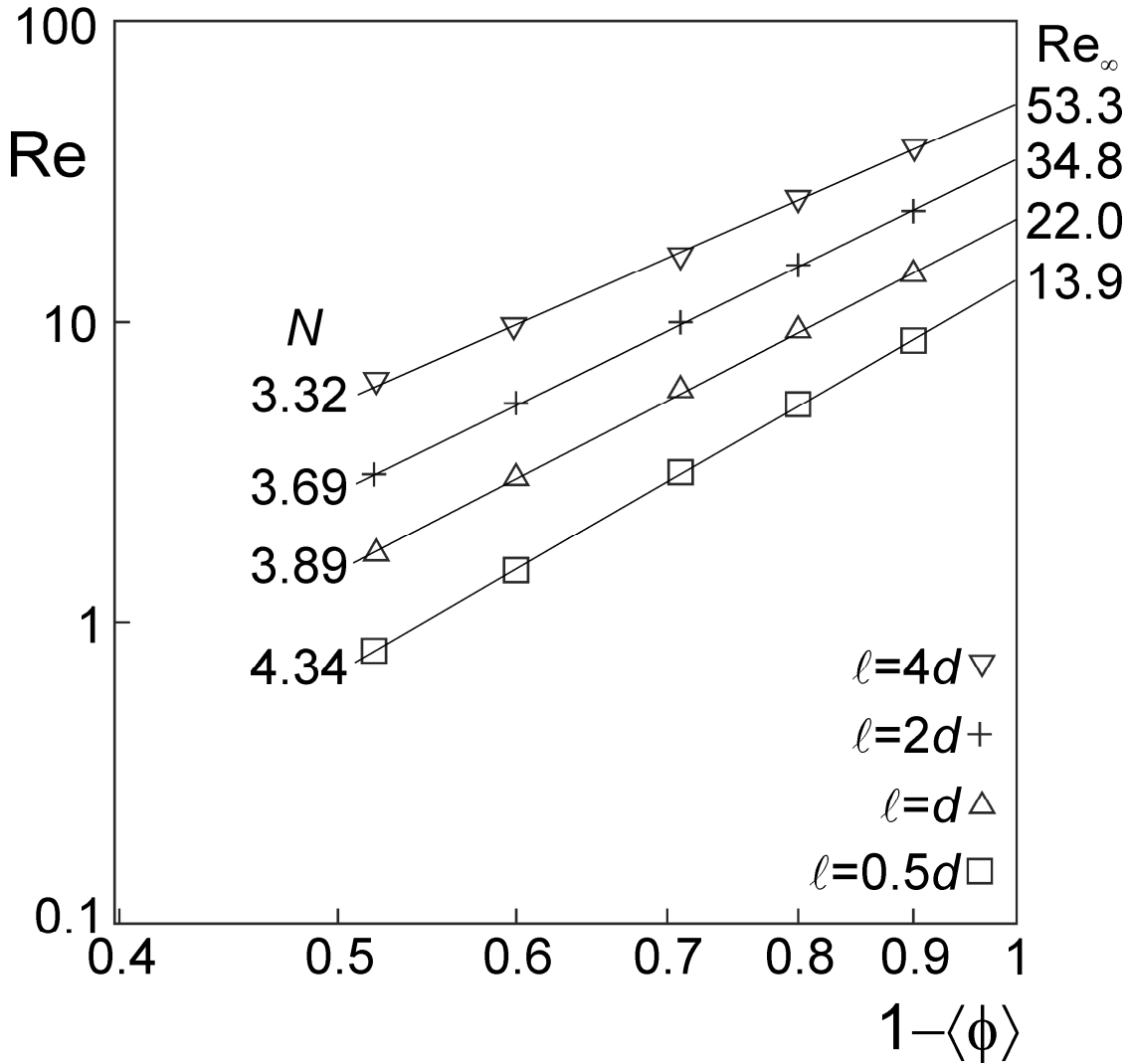


Figure 7. Distributions of the angles φ between cylinder centerlines and the vertical for all 20 cases represented in Figure 6 on hindered settling. The drawn black curve in each panel is $\sin\varphi$ which is representative for a random orientation distribution.

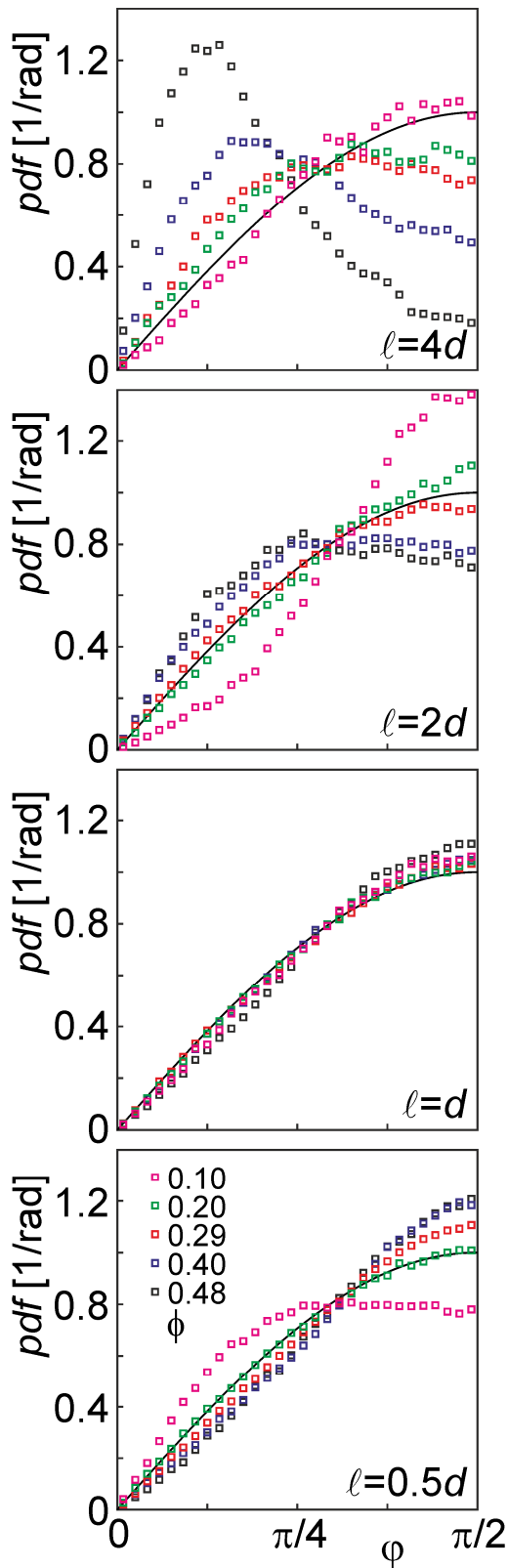


Figure 8. Particle velocity distribution functions. Top: $\ell/d=2$; bottom: $\ell/d=4$. The left panels show a comparison between horizontal (xy) and vertical (z) velocities at $\langle\phi\rangle=0.29$. The right panels show a comparison between vertical particle velocity distributions for various $\langle\phi\rangle$.

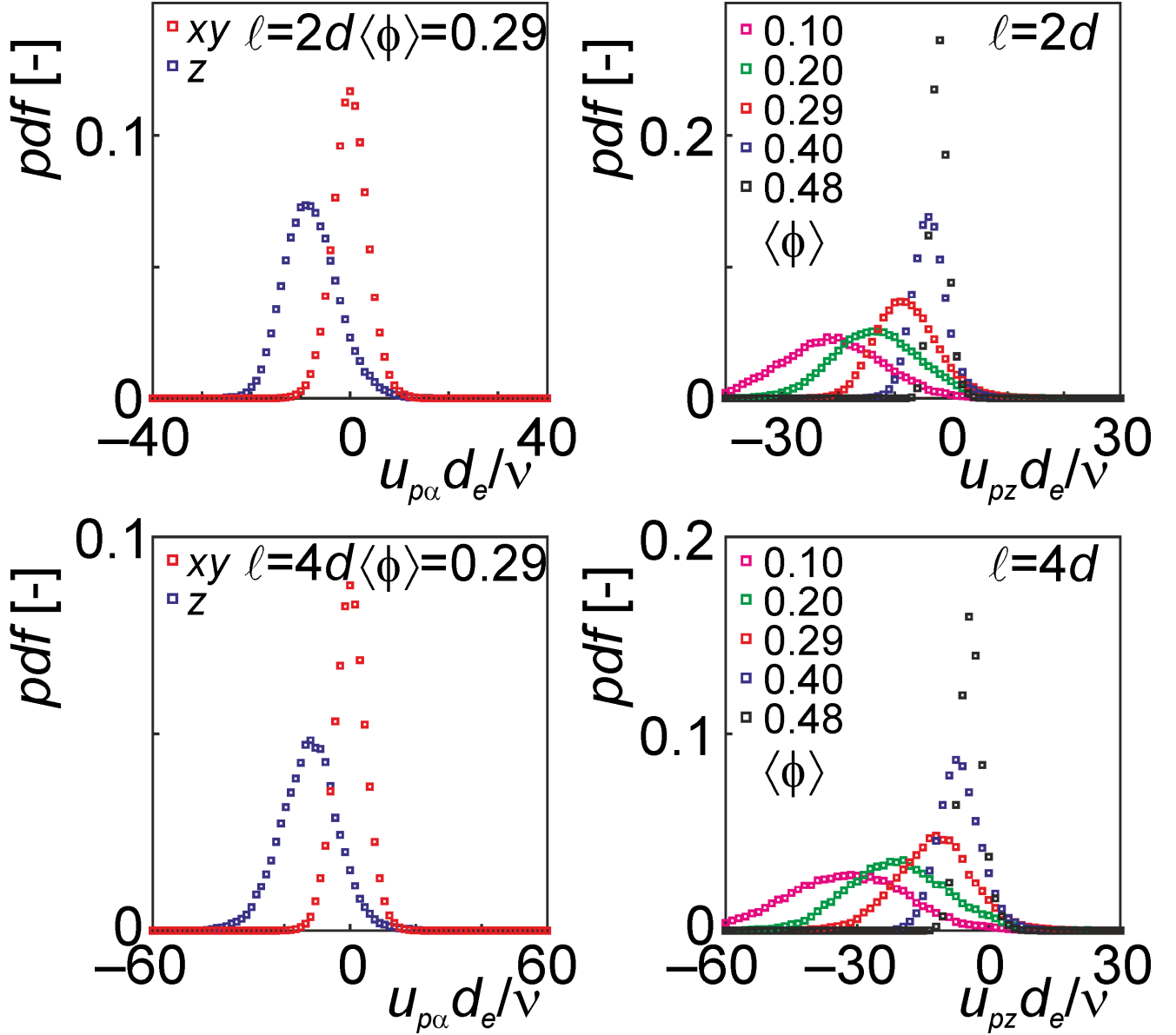


Figure 9. Particle velocity fluctuation levels $u'_{p\alpha} = \sqrt{\langle u_{p\alpha} - \langle u_{p\alpha} \rangle \rangle^2}$ normalized by the average settling velocity $u_{stl} = \left| \langle u_z \rangle - \langle u_{pz} \rangle \right|$ as a function of solids volume fraction for all cases considered in Figure 6 (on hindered settling). Red symbols indicate vertical (z) velocity fluctuations, black symbols horizontal (xy) fluctuations.

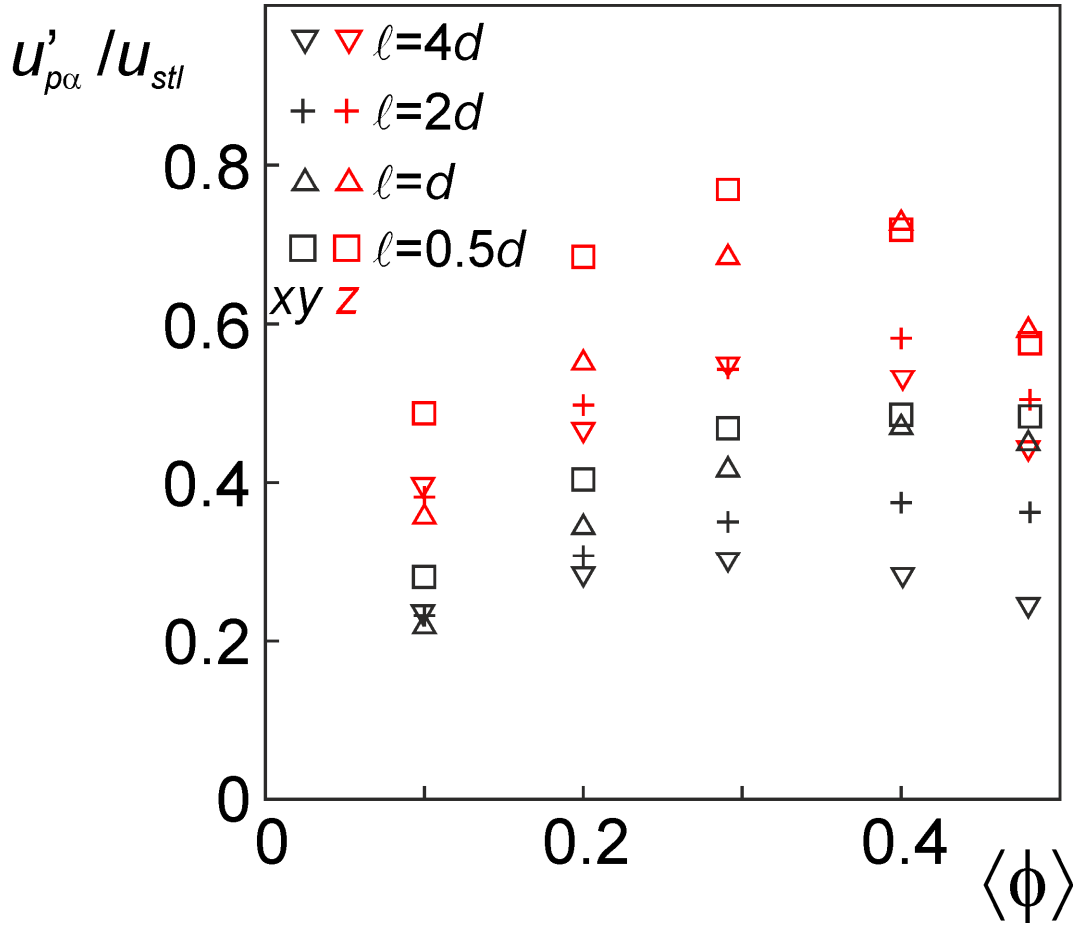


Figure 10. Hindered settling. Slip velocity Reynolds number as a function of $1-\langle\phi\rangle$ for various ℓ/d as indicated. Different from Figure 6, now all simulations have the same Galilei number based on the equivalent diameter: $Ga_e=1296$. Top and bottom panel have the same data on a logarithmic and linear Re scale respectively. $nx/d=9$, $d/\Delta=16$, $\nu=0.04$ (lattice units) for $\langle\phi\rangle\leq 0.40$ and $\nu=0.06$ for $\langle\phi\rangle> 0.40$.

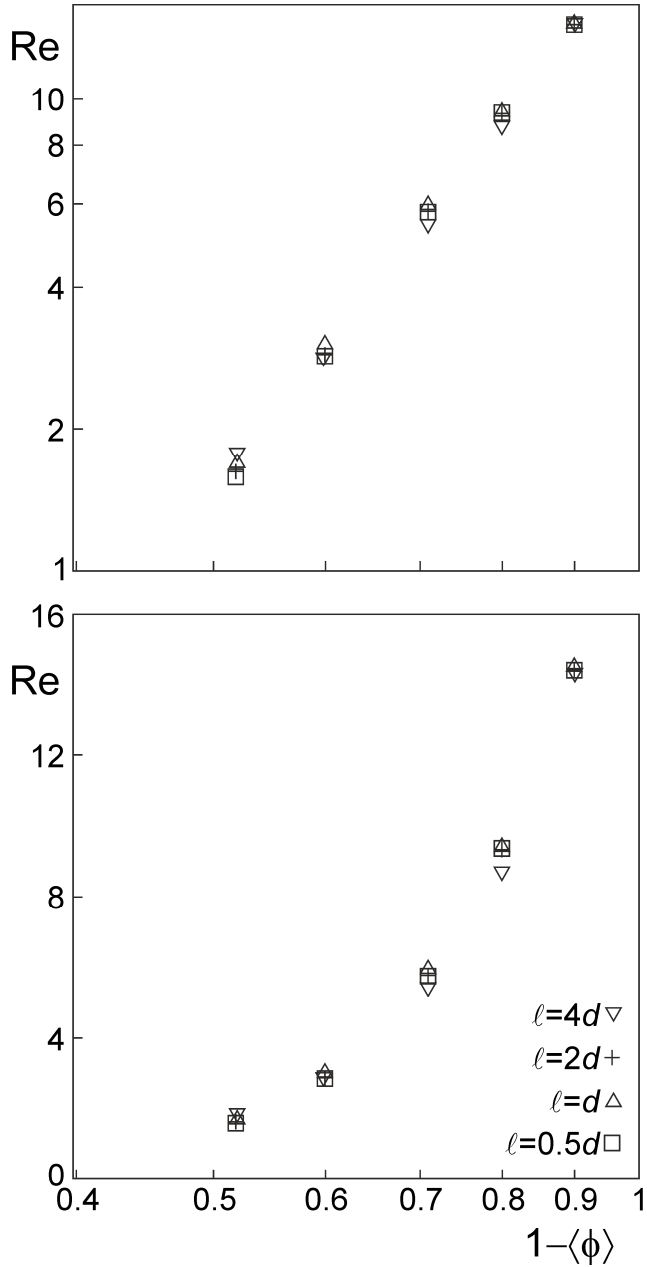


Figure 11. Distributions of the angles φ between cylinder centerlines and the vertical for all 20 cases represented in Figure 10 on hindered settling that all have $Ga_e=1296$. The drawn black curve in each panel is $\sin\varphi$ which is representative for a random orientation distribution.

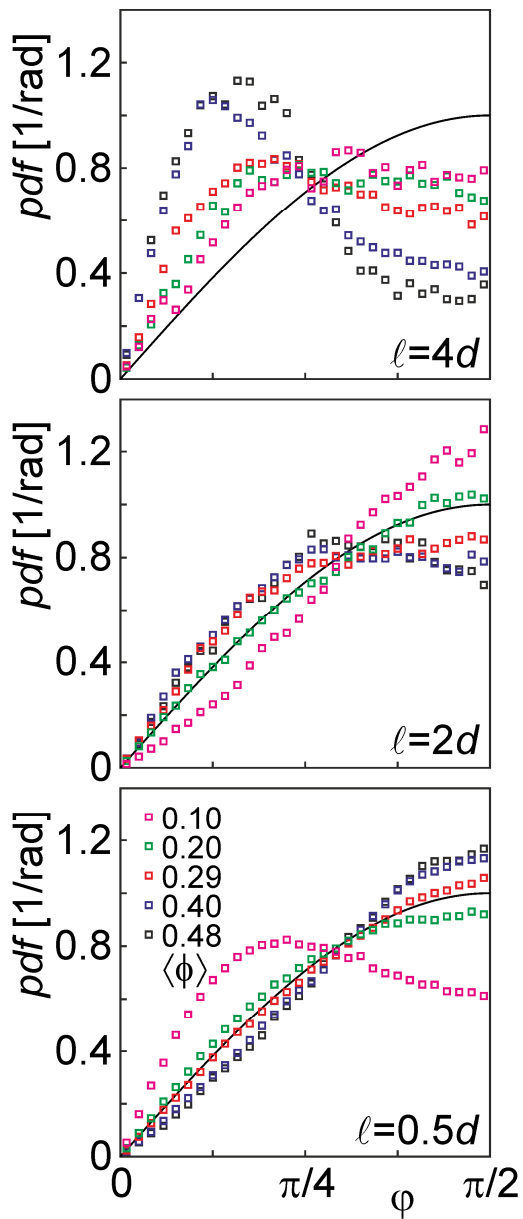
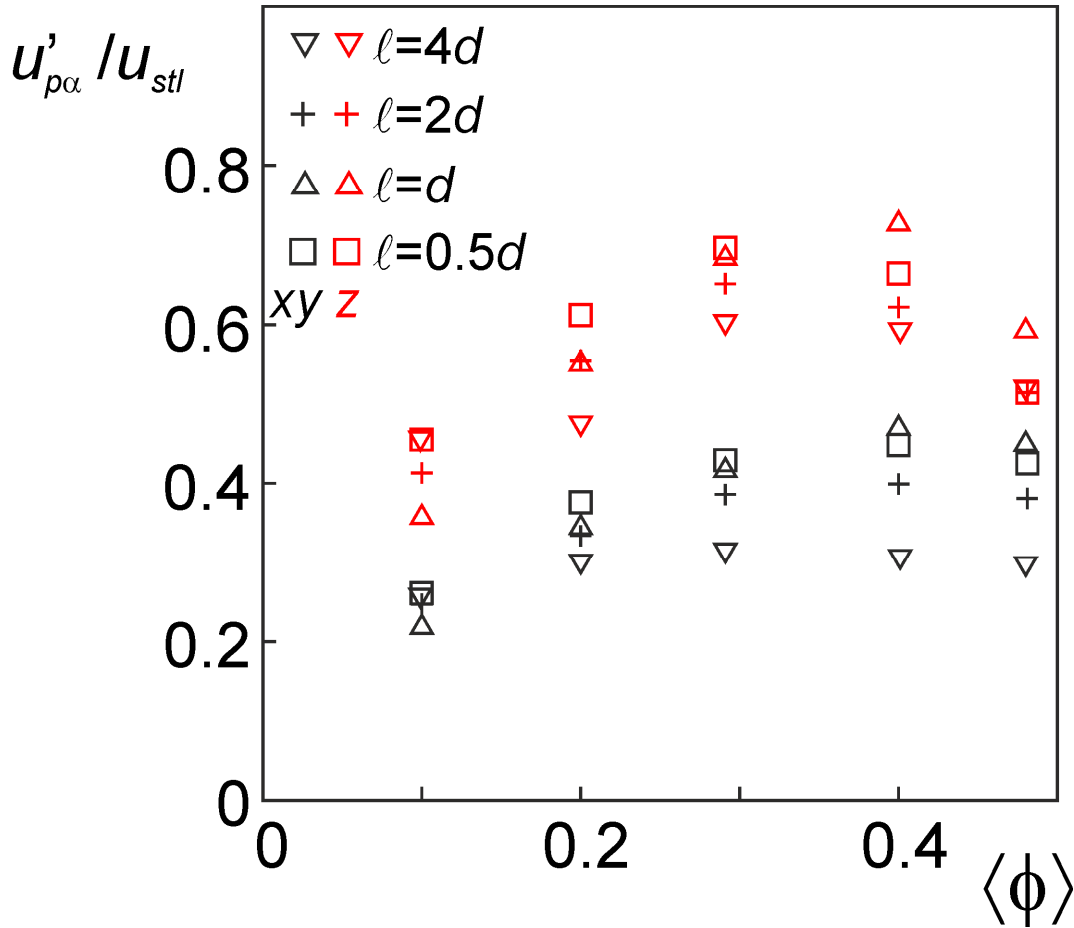


Figure 12. Particle velocity fluctuation levels $u'_{p\alpha} = \sqrt{\langle (u_{p\alpha} - \langle u_{p\alpha} \rangle)^2 \rangle}$ normalized by the average settling velocity $u_{stl} = \langle |u_z - \langle u_{pz} \rangle| \rangle$ as a function of solids volume fraction for all cases considered in Figure 10 with $Ga_e = 1296$. Red symbols indicate vertical (z) velocity fluctuations, black symbols horizontal (xy) fluctuations.



Tables

Table 1. Comparison of slip velocity Reynolds number (Re) and relative particle velocity fluctuation levels at $Ar_e = (\gamma - 1)gd_e^3/\nu^2 = 1296$ between simulations with (the default) density ratio 2.0 (blue font) and a density ratio such that the net gravity force on a single cylinder is the same irrespective of ℓ/d (red font).

Ar_e	ℓ/d	$\langle \phi \rangle$	ρ_p/ρ	Re	$u'_{pxy}/\langle u_{pz} \rangle$	$u'_{pz}/\langle u_{pz} \rangle$
1296	0.5	0.20	2.0	9.36	0.376	0.612
			3.0	9.33	0.368	0.583
		0.29	2.0	5.76	0.429	0.696
			3.0	5.76	0.422	0.670
		0.40	2.0	2.86	0.448	0.664
			3.0	2.86	0.458	0.678
	2.0	0.20	2.0	9.32	0.334	0.555
			1.5	9.24	0.333	0.539
		0.29	2.0	5.78	0.334	0.651
			1.5	5.74	0.364	0.622
		0.40	2.0	2.88	0.399	0.622
			1.5	2.89	0.405	0.612
4.0	0.20	2.0	8.59	0.294	0.568	
		1.25	8.53	0.294	0.543	
	0.29	2.0	5.32	0.308	0.596	
		1.25	5.41	0.325	0.634	
	0.40	2.0	2.78	0.300	0.586	
		1.25	2.88	0.310	0.663	